
Neural Multi-scale Image Compression

Ken Nakanishi¹ Shin-ichi Maeda² Takeru Miyato² Daisuke Okanohara²

Abstract

This study presents a new lossy image compression method that utilizes the multi-scale features of natural images. Our model consists of two networks: *multi-scale lossy autoencoder* and *parallel multi-scale lossless coder*. The multi-scale lossy autoencoder extracts the multi-scale image features to quantized variables and the parallel multi-scale lossless coder enables rapid and accurate lossless coding of the quantized variables via encoding/decoding the variables in parallel. Our proposed model achieves comparable performance to the state-of-the-art model on Kodak and RAISE-1k dataset images, and it encodes a PNG image of size 768×512 in 70 ms with a single GPU and a single CPU process and decodes it into a high-fidelity image in approximately 200 ms.

1. Introduction

Data compression for video and image data is a crucial technique for reducing communication traffic and saving data storage. Videos and images usually contain large redundancy, enabling significant reductions in data size via *lossy compression*, where data size is compressed while preserving the information necessary for its application. In this work, we are concerned with lossy compression tasks for natural images.

JPEG has been widely used for lossy image compression. However, the quality of the reconstructed images degrades, especially for low bit-rate compression. The degradation is considered to be caused by the use of linear transformation with an engineered basis. Linear transformations are insufficient for the accurate reconstruction of natural images, and an engineered basis may not be optimal.

In machine learning (ML)-based image compression, the compression model is optimized using training data. The concept of optimizing the encoder and the decoder model

¹The University of Tokyo ²Preferred Networks, Inc. Correspondence to: Ken Nakanishi <ken-nakanishi@g.ecc.u-tokyo.ac.jp>.

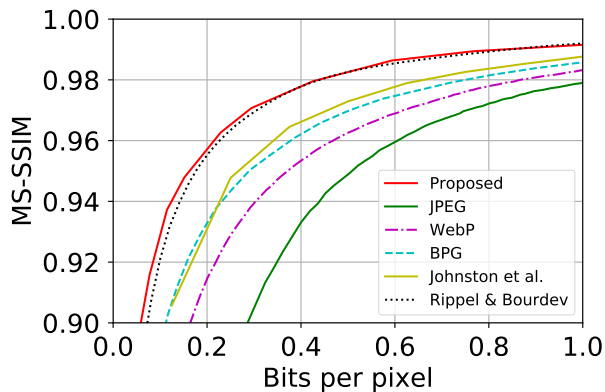


Figure 1. Rate-distortion trade off curves with different methods on Kodak dataset. The horizontal axis represents bits-per-pixel (bpp) and the vertical axis represents multi-scale structural similarity (MS-SSIM). Our model achieves better or comparable bpp with respect to the state-of-the-art results (Rippel & Bourdev, 2017).

via ML algorithm is not new. The K -means algorithm was used for vector quantization (Gersho & Gray, 2012), and the principal component analysis was used to construct the bases of transform coding (Goyal, 2001). However, their representation power was still insufficient to surpass the performance of the engineered coders. Recently, several studies proposed to use convolutional neural networks (CNN) for the lossy compression, resulting in impressive performance regarding lossy image compression (Toderici et al., 2015; 2017; Ballé et al., 2017; Theis et al., 2017; Johnston et al., 2017; Rippel & Bourdev, 2017; Mentzer et al., 2018) by exerting their strong representation power optimized via a large training dataset.

In this study, we utilize CNNs, but propose different architectures and training algorithm than those of existing studies to improve performance. The performance targets are two-fold, 1. *Good rate-distortion trade-off* and 2. *Fast encoding and decoding*. To improve these two points, we propose a model that consists of two components: *multi-scale lossy autoencoder* and *parallel multi-scale lossless coder*. The former, multi-scale lossy autoencoder extracts the multi-scale structure of natural images via multi-scale coding to achieve better rate-distortion trade-off, while the



Figure 2. Original and reconstructed images by our model.

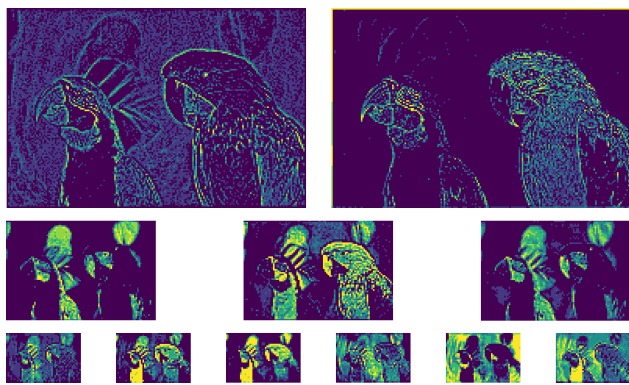


Figure 3. Visualization of quantized features, \hat{z} , at each resolution layer. Each panel represents the heatmap of \hat{z} at each resolution layer, where the top, middle, and bottom panels correspond to the map of the 1st, 2nd, and 3rd finest resolution layers. The value of \hat{z} in case of yellow-colored pixels is relatively high compared with the dark blue-colored pixels.

latter, parallel multi-scale lossless coder facilitates the rapid encoding/decoding with minimal performance degradation. We summarize the core concepts of each component of the model below.

- Multi-scale lossy autoencoder.** When we use a multi-layer CNN with pooling operation and/or strided convolution in this model, the deeper layers will obtain more global and high-level information from the image. Previous works (Toderici et al., 2015; 2017; Ballé et al., 2017; Theis et al., 2017; Johnston et al., 2017; Rippel & Bourdev, 2017; Mentzer et al., 2018) only used the features present at the deepest layer of such CNN model for encoding. In contrast, our lossy autoencoder model comprises of connections at different depths between the analyzer and the synthesizer, enabling encoding of multi-scale image features (See Fig. 5). Using this architecture, we can achieve a high compression rate with precise localization.
- Parallel multi-scale lossless coder.** Existing studies rely on sequential lossless coder, which makes the encoding/decoding time prohibitively large. We consider concepts for parallel multi-scale computations based on the version of PixelCNN used in (Reed et al., 2017) to enable encoding/decoding \hat{z} in a parallel manner; it achieves both fast encoding/decoding of \hat{z} and a high compression rate.

Our proposed model compresses Kodak¹ and RAISE-1k (Dang-Nguyen et al., 2015) dataset images into significantly smaller file sizes than JPEG, WebP, or BPG on fixed quality reconstructed images and achieves comparable rate distortion trade-off performance with respect to the state-of-the-art model (Rippel & Bourdev, 2017) on the Kodak and RAISE-1k datasets (See Figs. 1 and 8). Simultaneously, the proposed method achieves reasonably fast encoding and decoding speeds. For example, our proposed model encodes a PNG image of size 768×512 in 70 ms with a single GPU and a single CPU process and decodes it into a high-fidelity image with an MS-SSIM of 0.96 in approximately 200 ms. Two examples of reconstruction images by our model with an MS-SSIM of approximately 0.96 are shown in Fig. 2.

2. Proposed method

2.1. Overview of proposed architecture

In this section we first formulate the lossy compression. Subsequently, we introduce our lossy auto-encoder and lossless coder. Let the original image be x , the binary representation of the compressed variable be s , and the reconstructed image from s be \hat{x} . The objective of the lossy image com-

¹<http://r0k.us/graphics/kodak/>.

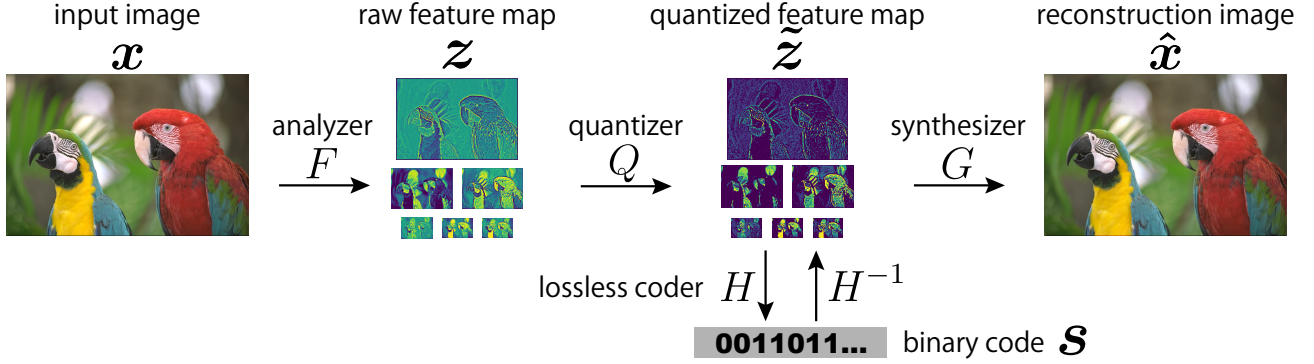


Figure 4. Overall architecture of proposed model. Our model consists of a lossy auto-encoder and a lossless coder where the lossy autoencoder consists of analyzer F , quantizer Q , and synthesizer G . The analyzer F converts image x to a feature map z . The quantizer module Q converts the feature map z to the quantized feature map \tilde{z} . The synthesizer G converts the quantized feature map \tilde{z} to a reconstruction image \hat{x} . The lossless coder H compresses the quantized feature map \tilde{z} to a binary code s , losslessly. H^{-1} is the inverse function of the lossless coder H .

pression is to minimize the code length (i.e., file size) of s while minimizing the distortion between x and \hat{x} : $d(x, \hat{x})$ as much as possible. The selection of the distortion $d(\cdot, \cdot)$ is arbitrary as long as it allows differentiation with respect to the input image.

Our model consists of a lossy auto-encoder and a lossless coder as shown in Fig. 4. The auto-encoder transforms the original image x into the features z using the analyzer F as $z = F(x; \phi)$. Subsequently, the features are quantized using a quantizer Q as $\tilde{z} = Q(z)$. Q quantizes each element of \tilde{z} using a multi-level uniform quantizer, which has no learned parameters. Finally, the synthesizer G of the auto-encoder, recovers the reconstructed image, $\hat{x} = G(\tilde{z}; \theta)$. Here, ϕ and θ are the parameters of F and G , respectively. Parameters θ and ϕ are optimized to minimize the following distortion loss:

$$L(\theta, \phi) := \mathbb{E}_{p(x)} [d(x, G(Q(F(x; \phi)); \theta))], \quad (1)$$

where $\mathbb{E}_{p(x)}[\cdot]$ represents the expectation over the input distribution, which is approximated by an empirical distribution.

The second neural network is used for the lossless compression of the quantized features \tilde{z} . According to Shannon’s information theory, the average code length is minimized when we allocate the code length, $\log_2 p(\tilde{z})$ bits, for the signal \tilde{z} whose occurrence probability is $p(\tilde{z})$. Hence, we estimate the occurrence probability of \tilde{z} as $p(\tilde{z}; \omega)$ where ω is a parameter to be estimated. In this study, ω is estimated via maximum likelihood estimation. Thus, we minimize cross entropy between $p(\tilde{z})$ and $p(\tilde{z}; \omega)$, using the fixed analyzer and synthesizer:

$$H(p, p_\omega) := -\mathbb{E}_{p(\tilde{z})} [\log_2 p(\tilde{z}; \omega)]. \quad (2)$$

Note that our objective function for ϕ , θ , and ω can be easily extended to the rate-distortion cost function, a weighted sum of distortion loss (1), and cross entropy (2). Using the rate-distortion cost function, we can jointly optimize ϕ , θ , and ω , as in previous studies (Ballé et al., 2017; Theis et al., 2017; Mentzer et al., 2018). Nevertheless, we separately optimize them by first optimizing the distortion loss with respect to ϕ and θ . Subsequently, we optimize the cross entropy with respect to ω . This two-step optimization simplifies the optimization of the analyzer F . Because the derivative of the rate-distortion function with respect to the parameter of the analyzer, ϕ depends on the occurrence probability $p(\tilde{z}; \omega)$, the computation of the derivative requires time and becomes complex. Furthermore, it may consume excessive memory for the computation of the derivative when we optimize the parameters with large number of images. Optimization with the rate-distortion cost function could be a future direction of research to pursue further performance improvements.

2.2. Multi-scale Auto-encoder

In this section, we describe our proposed auto-encoder. Our multi-scale auto-encoder consists of an analyzer F , a synthesizer G , and a quantizer Q . Both the analyzer F and synthesizer G are composed of CNNs similar to the existing studies. The difference between the proposed and existing models is that our auto-encoder encodes information of the

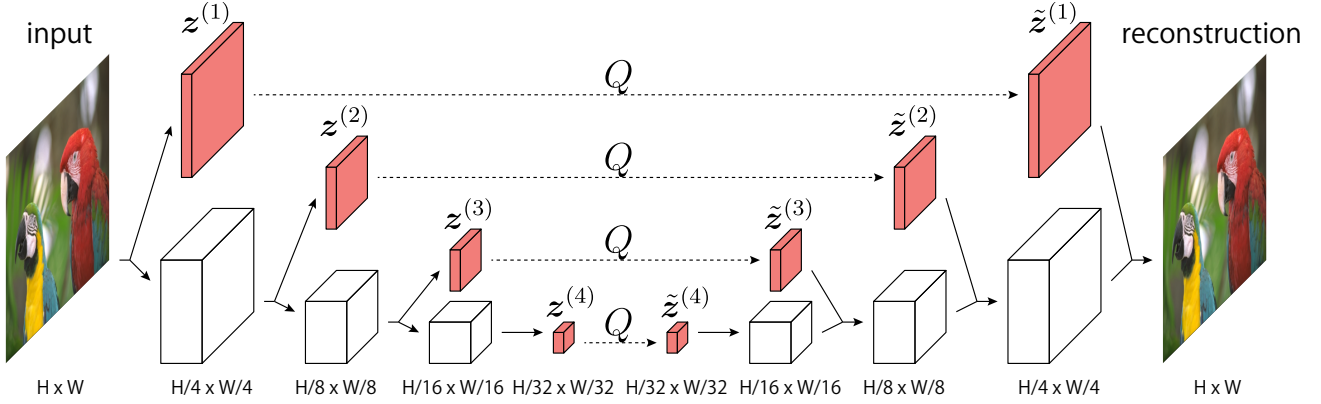


Figure 5. Architecture of our multi-scale autoencoder. H and W are height and width of an input image, respectively. The left side of the network is the analyzer F , and the right side is the synthesizer G . Light and vivid red-colored boxes represent pre-quantized variables z , and quantized variables \tilde{z} . The analyzer F and synthesizer G are described in Section 2.2. Quantizer module Q is described in Section 2.2.1.

original image in multi-scale features, as follows.

$$F : \mathbf{x} \mapsto \{z^{(i)}\}_{i=1}^M, \quad (3)$$

$$Q : \{z^{(i)}\}_{i=1}^M \mapsto \{\tilde{z}^{(i)}\}_{i=1}^M \quad (4)$$

$$G : \{\tilde{z}^{(i)}\}_{i=1}^M \mapsto \hat{\mathbf{x}}, \quad (5)$$

$$z^{(i)} \in \mathbb{R}^{C^{(i)} \times H^{(i)} \times W^{(i)}}, \quad (6)$$

$$\tilde{z}^{(i)} \in \{0, \dots, N-1\}^{C^{(i)} \times H^{(i)} \times W^{(i)}}, \quad (7)$$

where $z^{(i)}$ and $\tilde{z}^{(i)}$ denote the i -th ($i = 1, \dots, M$) resolution of features and its quantized version, whose spatial resolution is $H^{(i)} \times W^{(i)}$ and number of channels is $C^{(i)}$. The spatial resolution becomes coarser as the layer i becomes deeper, such that both $H^{(i)} > H^{(i+1)}$ and $W^{(i)} > W^{(i+1)}$ hold. Each element of \tilde{z} is quantized into $\{0, \dots, N-1\}$, $N \in \mathbb{N}$. Fig. 5 shows an example of $M = 4$. Global and coarse information including textures, are encoded at the deeper layer, whereas local and fine information, such as edges, are encoded at the shallower layer. The parameters of F and G , ϕ and θ , are trained to minimize distortion loss (1).

2.2.1. QUANTIZER MODULE

Because quantization is not a differentiable operation, it makes optimization difficult. Recent studies (Ballé et al., 2017; Toderici et al., 2017; Johnston et al., 2017; Agustsson et al., 2017) have used stochastic perturbations to avoid the problem of non-differentiability. They replace the original distortion loss with the average distortion loss where the distortion occurs owing to the injection of the stochastic perturbation to the feature maps, instead of the deterministic quantization. In general, however, the stochastic perturbation makes the training longer, because we require considering samples with large size to approximate the expected

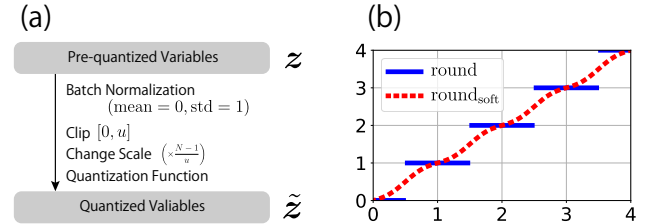


Figure 6. Quantizer module. Panel (a) shows quantization procedures and panel (b) shows $\text{round}(x)$ (blue dashed line) and the plot of $\text{round}_{\text{soft}}(x)$ (red solid line), which are used as a hard quantization function and a soft quantization function, respectively.

value .

To avoid complexity of optimization when injecting stochastic perturbation, we adopt deterministic quantization even during training, similar to the recent work (Mentzer et al., 2018). The quantizer module we use is shown in Fig. 6.

Before quantization, we apply several preprocessing steps on z . First, to enhance the compression rate of the lossless coding, we apply batch normalization (BN) on z , which drives the statistics of the feature map to exhibit zero mean and unit variance. BN makes each channel of z possess similar statistics to each other, which is beneficial for estimating the probability of the discretized feature map $p(\tilde{z}; \omega)$ using which CNN shares internal layer except for the top layer. Additionally, the control of statistics via BN is advantageous for decreasing the entropy of \tilde{z} . Subsequently, we clip the normalized z into $[0, u]$ ($u > 0$) and expand its range into $[0, N-1]$ via multiplying $\frac{N-1}{u}$. In this study, we set $u = 4$.

Following the above mentioned preprocessing, we apply

multi-level quantization:

$$\text{round}(x) = \lceil x - 0.5 \rceil, \quad (8)$$

where $\lceil a \rceil$ is a ceiling function that yields the smallest integer, which is larger than or equal to a . This quantization function is not differentiable and does not allow conduction of the gradient-based optimization. To overcome this difficulty, we consider a similar strategy as Mentzer et al. (2018). We replace the quantization function with the ‘‘soft’’ quantization function when computing back-propagation, while the intact quantization function is used to compute forward propagation. The soft quantization function we used is written as

$$\text{round}_{\text{soft}}(x) = x - \alpha \frac{\sin(2\pi x)}{2\pi}, \quad (9)$$

where we used $\alpha = \frac{1}{2}$. Fig. 6 (b) shows $\text{round}_{\text{soft}}(x)$ (Eq. (9)) overlaid on $\text{round}(x)$ (Eq. (8)). Owing to this approximation, we can conduct conventional gradient-based optimization for the minimization of the distortion loss (Eq. (1)) with respect to θ and ϕ and the usual training of the neural network. Although this gradient-based optimization uses improper gradient, the performance of our model is comparable or superior to the performance of existing models, as demonstrated in our experiment, implying that the side effect is not prominent.

2.3. Parallel Multi-scale Lossless Coder

In this section, we explain the construction of lossless coding, $H: \tilde{z} \mapsto s$, that transmits the multi-scale feature map \tilde{z} into a one-dimensional binary sequence s .

To minimize average code length, we estimate the occurrence probability of \tilde{z} . Suppose \tilde{z} is indexed in raster scan order as $\tilde{z} = (z_1, \dots, z_I)$ where $I = \sum_{i=1}^M C^{(i)} \times H^{(i)} \times W^{(i)}$. Subsequently, the joint probability $p(\tilde{z})$ is represented as the product of the conditional distributions:

$$p(\tilde{z}) = p(z_1) \prod_{i=2}^I p(z_i | z_1, \dots, z_{i-1}). \quad (10)$$

Conveniently, the problem of learning the conditional distribution can be formulated as a supervised classification task, which is successfully solved via neural networks. If z_i takes one of N -values, the neural network that contains N -output variables is trained to predict the value (i.e., label) of z_i . Subsequently, the output of the trained neural network mimics $p(z_i | z_1, z_2, \dots, z_{i-1})$. The estimated probability is used for encoding z_i , as illustrated in Fig. 7(a).

Toderici et al. (2017) used PixelRNN to learn $p(z_i | z_1, \dots, z_{i-1})$ ($i \geq 2$), demonstrating that it achieves a high theoretical compression rate. In practice, however, it requires a long computational time for both

encoding and decoding, proportional to the number of elements of \tilde{z} , because PixelRNN sequentially encodes z_i .

To reduce the computation time for both encoding and decoding, we use a parallel multi-scale PixelCNN (Reed et al., 2017). The concept behind this model is to take advantage of conditional independence. We divide the elements of \tilde{z} into K subsets $v^{(k)}$ ($k = 1, 2, \dots, K$), where the k -th subset includes I_k elements. We subsequently assume the conditional independence among the elements of the subset. Namely, we assume that $p(\tilde{z})$ is represented as

$$p(\tilde{z}) \simeq p(v^{(1)}) \prod_{k=2}^K \prod_{i=1}^{I_k} p(v_i^{(k)} | v^{(1)}, \dots, v^{(k-1)}). \quad (11)$$

Although conditional independence does not hold in general, it significantly reduces the computation time, because the number of evaluations of neural networks is no longer proportional to the number of elements N , but is instead proportional to the number of subsets K , where, typically, $K \ll N$.

Specifically, we assume conditional independence in spatial and channel domain as conducted in Reed et al. (2017), but with a slightly different implementation. Because we use CNN as the analyzer and synthesizer of the autoencoder, the feature map \tilde{z} preserves the spatial information. The spatial correlation between pixels of \tilde{z} tends to decrease as the distance increases. Thus, we assume the conditional independence between the distant units in the feature map when conditioned on the relatively close units in the feature map. This is illustrated in Figs. 7(b)-(d), where the red units are assumed to be independent from each other under the condition that the dark-gray units are provided. We simply consider a single resolution case; the multi-resolution case is explained in appendix. Encoding the red units given the dark-gray units, as in the order of Fig. 7 (b) and (c), we can encode denser units, based on the given sparser units. Iterating this procedure, as shown in Fig. 7 (d), we can encode all the units of \tilde{z} , given $v^{(1)}$. To encode $v^{(1)}$, we simply assume independence among the units in $v^{(1)}$ and assume it obeys an identical distribution, irrelevant to the spatial position. Subsequently, we estimate the histogram to approximate the distribution.

3. Comparison with existing CNN-based lossy image compression

In this section, we review recent studies regarding CNN-based image compression to elucidate the value of our contribution. CNN-based image compression exhibits high image compression performance. It also achieves better visual quality of reconstruction, especially on low bit-rate compression, compared with classic compression methods, such as JPEG.

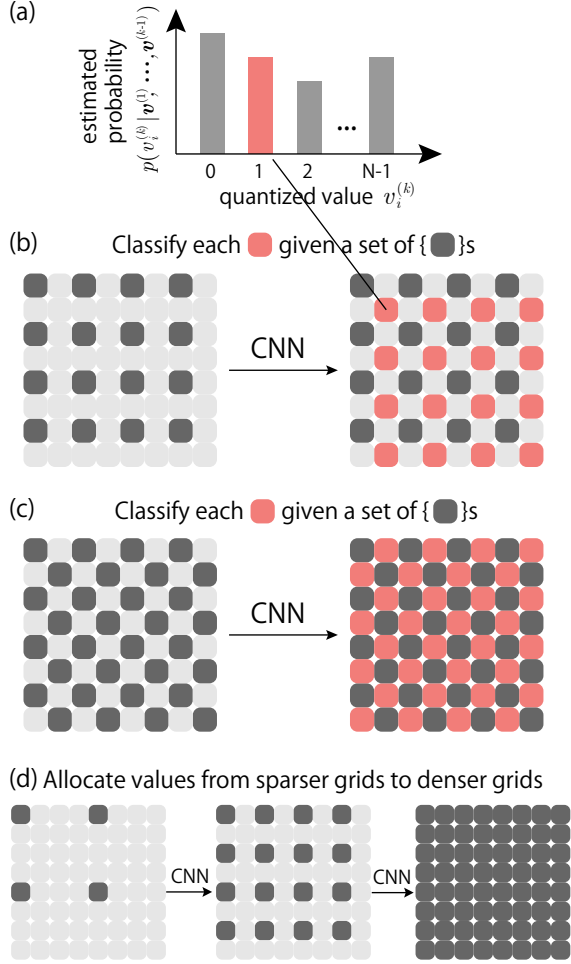


Figure 7. Lossless coding with parallel multi-scale PixelCNN. (a) The conditional probability estimated by CNN is used to encode the i -th quantized feature $v^{(i)}$; (b),(c) two types of conditional independence in spatial domain are assumed, and each distribution is estimated by solving the classification task with CNN; and (d) the values of dense grids are encoded by conducting procedures (b) and (c), iteratively.

For the entropy coding, Ballé et al. (2017) and Theis et al. (2017) modeled $p(\tilde{z})$ using a factor of independent probability distributions (i.e., $p(\tilde{z}; \omega) := \prod_i p(z_i; \omega_i)$). However, this could result in poor accuracy regarding the entropy estimation, because spatial neighborhood pixels are generally highly correlated and independent assumption causes over-estimation of the entropy. To solve this problem, Li et al. (2017); Rippel & Bourdev (2017); Mentzer et al. (2018) constructed a model of probability distribution for each quantized variable, given their neighborhoods. This model is called *context model*. However, via construction, using such a context model requires sequential encoding/decoding over \tilde{z} , thus the encoding/decoding speed significantly slows down when a computationally heavy model, such as PixelCNN (Oord et al., 2016), is used for

the context model. To reduce the computational cost for the encoding/decoding, Li et al. (2017); Mentzer et al. (2018) used learned *importance masks* models on \tilde{z} , to adaptively skip the encoding/decoding by observing each estimated importance mask on each element of \tilde{z} . Mentzer et al. (2018) achieved state-of-the-art performance using PixelCNN as the context model. However, it still requires sequential encoding/decoding over \tilde{z} .

In contrast, our proposed model exhibits parallel encoding/decoding over a subset of \tilde{z} assuming the conditional independence. Our assumption of the conditional independence reflects the property of the natural image statistics, i.e., the spatial correlation between pixels decreases as the pixels are distant from each other. The conditional independence allows to sample \tilde{z} in a parallel manner, thus, our model can perform fast encoding/decoding with a GPU. Reed et al. (2017) demonstrated that such a parallel multi-scale density model achieves comparative performance with respect to the original PixelCNN, thus we can expect our proposed model to achieve both fast encode/decoding and accurate entropy coding.

Regarding the architecture of lossy autoencoder, to the best of our knowledge, all the existing studies used variants of the autoencoder, which exhibits a bottleneck at the deepest layer of the encoder. Although the proposed architecture possesses a similar structure as in the existing studies (Ronneberger et al., 2015; Rippel & Bourdev, 2017) in the sense that the analyzer and the synthesizer exhibit symmetric structures, our model is specialized for lossy image compression where each feature map of the analyzer is quantized and stored to maintain the various resolutions of image features. This is not explored in existing studies where the quantization is applied to the deepest layer (Ballé et al., 2017; Theis et al., 2017; Johnston et al., 2017; Mentzer et al., 2018) or applied after taking the sum of multiple features (Rippel & Bourdev, 2017). Toderici et al. (2015; 2017) proposed a different architecture compared with the standard lossy autoencoder we have described here, to realize variable compression rate regarding neural compression. Their lossy compression model consists of recurrent neural network-based encoder and decoder. In each recurrence, the encoder considers the difference of each pixel between the original image and its reconstruction as an additional input to the originals, and the encoder and decoder are trained so as to minimize the distortion loss. Their proposed model, however, consumes significant computational time for encoding/decoding, compared with the standard lossy autoencoder model, owing to its nature of sequential recurrent computation.

4. Experiments

4.1. Experimental setup

We conducted experiments to evaluate the image compression performance of our model regarding benchmark datasets. We compared the performance with existing file formats, JPEG, WebP, BPG, and state-of-the-art neural compression methods (Johnston et al., 2017; Rippel & Bourdev, 2017).

For the training dataset, we used Yahoo Flickr Creative Commons 100M (Kalkowski et al., 2015), which has been used in the study regarding the current state of the art method (Rippel & Bourdev, 2017). The original dataset consists of 100-million images. We selected portions of images whose both vertical and horizontal resolution were greater than or equal to $1,024 \times 1,024$. We used 95,205 selected images for training and 1,000 selected images for validation. For pre-processing of the lossy autoencoder training, we resized the images into those whose short sides were 512. Subsequently, we cropped the resized images to 512×512 . For the lossless coder training, we performed the same pre-processing as for the lossy autoencoder, except that our resizing and cropping size was $1,024 \times 1,024$. We used (negative) MS-SSIM (Wang et al., 2004) for the distortion loss (1), which is observed to exhibit high correlation with human subjective evaluation. It is commonly used to evaluate the quality of the image compression. Please refer to the appendix for further details of the experiments.

4.2. Comparison of the compression performances

Fig. 1² shows the RD curves with different compression methods on the Kodak dataset. Our proposed model achieved superior performance to the existing file formats, JPEG³, WebP⁴, and BPG⁵.

Moreover, the proposed model achieved better performance than nearly all the existing neural compression methods (Toderici et al., 2017; Ballé et al., 2017). It demonstrated comparable performance with respect to recent CNN-based compression (Rippel & Bourdev, 2017). When we compare the RD-curve carefully with Rippel & Bourdev (2017), it seems that our method is advantageous in case of wide range of low bit-rates. Refer to appendix for certain reconstructed

²Regarding the RD curves of Rippel & Bourdev (2017), we carefully traced the RD curve from the figure of their paper, because we could not obtain the exact values at each point. As for the RD curve of Johnston et al. (2017), we used the points provided by the authors via personal communication. The exact values of bpp and MS-SSIM on the RD curve of the proposed method are shown in Table 1 in appendix.

³<http://www.ijg.org/>

⁴<https://developers.google.com/speed/webp/>

⁵<https://bellard.org/bpg/>

images on the Kodak dataset.

Fig. 8 shows the RD curves on the RAISE-1k dataset. Our model also achieves superior performance over the other methods.

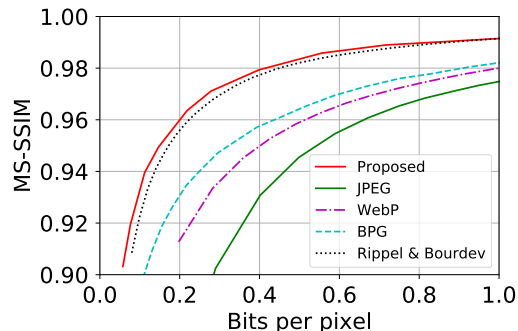


Figure 8. Rate-distortion trade-off curves with different methods on the RAISE-1k dataset.

To evaluate the encoding and decoding speeds of our model, we compare the computation time for encoding and decoding against JPEG, WebP, and BPG. Unfortunately, we cannot implement the state-of-the-art DNN-based study (Rippel & Bourdev, 2017) because the detail of the architecture and lossy compression procedures are not written in their paper.

As for the computational resources, our proposed model operated on a single GPU and a single CPU process, whereas JPEG, WebP, and BPG used a single CPU process. We used PNG file format as original images because it is a widely accepted file format and publicly available BPG codec, libbpg, only accepts either JPEG or PNG file format as the input. To achieve a fair comparison, we measured the computation time including the decoding of PNG-format image into Python array, and encoding process from Python array into the binary representations (encoding time), and the time required for decoding from the binary representations into the PNG-format image (decoding time). Note that the transformation between a PNG-format image and a GPU array was not optimized with respect to the computation time; we did not transform each PNG-format image into a cuda array on GPU directly⁶. The direct transformation, which would reduce the computation time of our model, is reserved for future study.

Fig. 9 shows the computational times for encoding and decoding. For encoding, our proposed method takes approximately 0.1 s or less than 0.1 s for the region where the MS-SSIM takes less than 0.98. It is significantly faster than BPG, but inferior to JPEG and WebP. Note that a re-

⁶We first transformed the PNG-format image into a numpy array on CPU with the python library ‘Pillow’, then transferred it to a cuda array on GPU.

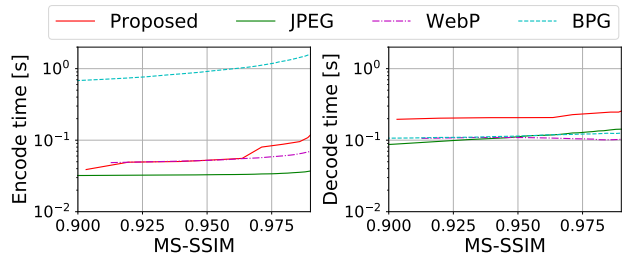


Figure 9. Computational time vs. MS-SSIM plots on the RAISE-1k dataset. The left and right panel indicate the results of the encoding time and decoding time, respectively.

constructed image with an MS-SSIM of 0.96 is usually a high-fidelity image, which is difficult to distinguish from the original image by human eyes. Two examples of our reconstructed image are shown in Fig. 2. The MS-SSIM of the top and bottom reconstructed image are 0.961 and 0.964, respectively. The decoding time of our proposed method is approximately 0.2 s for the range of MS-SSIM between 0.9 to 0.99. It is nearly two times slower than the other file formats.

4.3. Analysis by ablation studies

We conducted ablation experiments to indicate the efficacy of each of our proposed modules: multi-scale lossy autoencoder and parallel multi-scale lossless coder.

4.3.1. PARALLEL MULTI-SCALE LOSSLESS CODER VS. INDEPENDENT LOSSLESS CODER

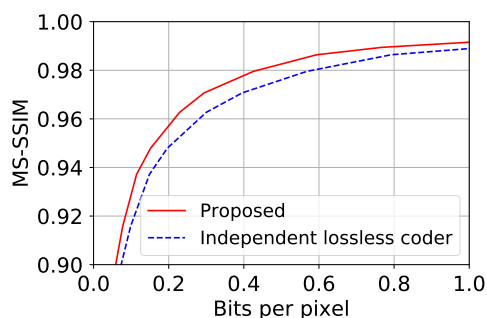


Figure 10. Entropy coding by proposed parallel multi-scale lossless coder vs. independent lossless coder.

Here, we discuss the efficacy of our lossless coder against an *independent lossless coder* that conducts lossless coding of each element of \tilde{z} by observing the histograms of each channel of \tilde{z} . As for the lossy autoencoder model, we used architecture identical to the proposed model. Fig. 10 shows the RD-curves with respect to our lossless coder and independent lossless coder (Ballé et al., 2017; Theis et al., 2017). We can observe that our lossless coder achieved sig-

nificantly better performance than the independent lossless coder. Note that, evidently, the independent lossless coder can encode/decode faster compared with our lossless coder.

4.3.2. MULTI-SCALE VS. SINGLE-SCALE AUTOENCODER

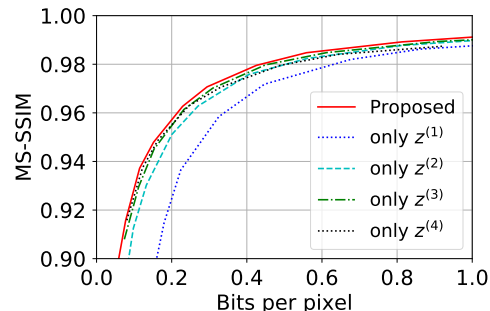


Figure 11. Multi-scale vs. single-scale autoencoder. RD-curves of our proposed model (multi-scale autoencoder) are compared with that of single-scale autoencoders. Each single-scale autoencoder possesses architecture identical to the proposed model, but the quantization is applied to the units only at specific depth of the layer. “only $z^{(i)}$ ” in the legend refers to the single-scale autoencoder that is quantized only at the i -th layer units.

Fig. 11 shows the RD-curves on multi-scale (i.e., proposed) and single-scale autoencoders. Each single-scale autoencoder possess architecture identical to the proposed model, except it only possess only one connection at specific depth of the layer. As for the structure of each single-scale autoencoder, we used the architecture identical to the proposed model, except that the quantization is applied at a specific depth of the layer. The deeper layers are not used for both encoding and decoding. The training was separately conducted to achieve the best performance for each single-scale autoencoder. In this experiment, the quantization level is always fixed at 7. As can be observed from the figure, our model certainly achieved better performance than other single-resolution autoencoder models at any bitrate, although, the gains are not so large. This may be because we did not conduct the joint optimization of the parameters of the lossy autoencoder and the lossless coder. The separate optimization may hinder exploitation of the benefits of multi-resolution features, because the entropy of the feature map would be different at each resolution, and the separate optimization makes it difficult to exploit the property.

Fig. 3 shows the quantized feature map at each layer, obtained via our lossy autoencoder. We observe that each quantized feature map extracts different scale of features. For example, the quantized feature maps at the high-resolution layer (top panels) encode the features in the high-frequency domain, including edges, whereas the quantized feature map at the low-resolution layer encodes the features in the low-frequency domain, including background colors and

surfaces.

5. Conclusion

In this study, we propose a novel CNN-based lossy image compression algorithm. Our model consists of two networks: *multi-scale lossy autoencoder* and *parallel multi-scale lossless coder*. The multi-scale lossy autoencoder extracts multi-scale features and encodes them. We successfully obtained different features of images. Local and fine information, such as edges, were extracted at the relatively shallow layer, and global and coarse information, such as textures, were extracted at the deeper layer. We confirmed that this architecture certainly improves the RD-curve at any bitrate. The parallel multi-scale lossless coder encodes the discretized feature map into compressed binary codes, and decodes the compressed binary codes into the discretized feature map in a lossless manner. Assuming the conditional independence and the parallel multi-scale pixelCNN (Reed et al., 2017), we encoded and decoded the discretized feature map in a partially parallel manner, making the encoding/decoding times significantly fast without losing much quality. Our experiments with the Kodak and RAISE-1k datasets indicated that our proposed method achieved state-of-the-art performance with reasonably fast encoding/decoding times. We believe our model makes the CNN-based lossy image coder step towards the practical uses that require high image compression quality and fast encoding/decoding time.

References

- Agustsson, Eirikur, Mentzer, Fabian, Tschannen, Michael, Cavigelli, Lukas, Timofte, Radu, Benini, Luca, and Gool, Luc V. Soft-to-hard vector quantization for end-to-end learning compressible representations. In *NIPS*, pp. 1141–1151, 2017.
- Ballé, Johannes, Laparra, Valero, and Simoncelli, Eero P. End-to-end optimized image compression. In *ICLR*, 2017.
- Dang-Nguyen, Duc-Tien, Pasquini, Cecilia, Conotter, Valentina, and Boato, Giulia. RAISE: A raw images dataset for digital image forensics. In *ACM Multimedia Systems Conference*, pp. 219–224, 2015.
- Gersho, Allen and Gray, Robert M. *Vector quantization and signal compression*, volume 159. Springer Science & Business Media, 2012.
- Goyal, Vivek K. Theoretical foundations of transform coding. *IEEE Signal Processing Magazine*, 18(5):9–21, 2001.
- Johnston, Nick, Vincent, Damien, Minnen, David, Covell, Michele, Singh, Saurabh, Chinen, Troy, Hwang, Sung Jin, Shor, Joel, and Toderici, George. Improved lossy image compression with priming and spatially adaptive bit rates for recurrent networks. *arXiv preprint arXiv:1703.10114*, 2017.
- Kalkowski, Sebastian, Schulze, Christian, Dengel, Andreas, and Borth, Damian. Real-time analysis and visualization of the yfcc100m dataset. In *Workshop on Community-Organized Multimodal Mining: Opportunities for Novel Solutions*, pp. 25–30, 2015.
- Kingma, Diederik and Ba, Jimmy. Adam: A method for stochastic optimization. In *ICLR*, 2015.
- Li, Mu, Zuo, Wangmeng, Gu, Shuhang, Zhao, Debin, and Zhang, David. Learning convolutional networks for content-weighted image compression. *arXiv preprint arXiv:1703.10553*, 2017.
- Mentzer, Fabian, Agustsson, Eirikur, Tschannen, Michael, Timofte, Radu, and Van Gool, Luc. Conditional probability models for deep image compression. *arXiv preprint arXiv:1801.04260*, 2018.
- Oord, Aaron van den, Kalchbrenner, Nal, and Kavukcuoglu, Koray. Pixel recurrent neural networks. In *ICML*, pp. 1747–1756, 2016.
- Reed, Scott, Oord, Aäron van den, Kalchbrenner, Nal, Colmenarejo, Sergio Gómez, Wang, Ziyu, Belov, Dan, and de Freitas, Nando. Parallel multiscale autoregressive density estimation. In *ICML*, pp. 2912–2921, 2017.
- Rippel, Oren and Bourdev, Lubomir. Real-time adaptive image compression. In *ICML*, pp. 2922–2930, 2017.
- Ronneberger, Olaf, Fischer, Philipp, and Brox, Thomas. U-net: Convolutional networks for biomedical image segmentation. In *International Conference on Medical Image Computing and Computer-Assisted Intervention*, pp. 234–241, 2015.
- Theis, Lucas, Shi, Wenzhe, Cunningham, Andrew, and Huszár, Ferenc. Lossy image compression with compressive autoencoders. In *ICLR*, 2017.
- Toderici, George, O’Malley, Sean M, Hwang, Sung Jin, Vincent, Damien, Minnen, David, Baluja, Shumeet, Covell, Michele, and Sukthankar, Rahul. Variable rate image compression with recurrent neural networks. *arXiv preprint arXiv:1511.06085*, 2015.
- Toderici, George, Vincent, Damien, Johnston, Nick, Hwang, Sung Jin, Minnen, David, Shor, Joel, and Covell, Michele. Full resolution image compression with recurrent neural networks. In *CVPR*, pp. 5435–5443, 2017.

Wang, Zhou, Simoncelli, Eero P, and Bovik, Alan C. Multi-scale structural similarity for image quality assessment. In *Conference Record of the Thirty-Seventh Asilomar Conference on Signals, Systems and Computers*, volume 2, pp. 1398–1402. IEEE, 2004.

A. Lossless encoding of multi-scale features

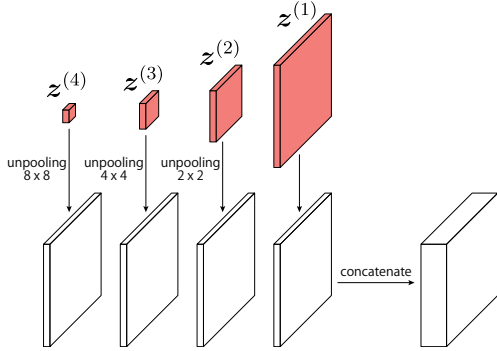


Figure 12. Integration of multi-scale feature map . The feature map is upsampled to maintain the same spatial resolution as the densest feature map obtained via unpooling. The upsampled feature map is accumulated and all channels are concatenated.

In our proposed architecture, several feature maps, each having different resolutions, are quantized. To encode different scaled feature maps, we upsample them, i.e., copy their values to the interpolated adjacent units (i.e., unpooling) so that all upsampled feature maps possess the same resolution as the densest feature map. Subsequently, the channels are accumulated with respect to the corresponding unit, as shown in Fig. 12. Next, the dark-gray units in Fig. 7 integrate the information of all the channels provided by all resolution feature maps. Similarly, the red units contain the information of all channels. Certain channels are shared between dark-gray units and red units because of unpooling. Thus, the non-trivial channels of red units, which are not shared with dark-gray units, are estimated for the training of the conditional distribution.

B. Detail of the experiment

B.1. Evaluation method

Regarding the distortion loss (1), we used MS-SSIM (Wang et al., 2004), which is demonstrated to exhibit high correlation with human subjective evaluation. It is commonly used to evaluate the quality of the image compression. MS-SSIM was originally designed for single channel images. To use MS-SSIM for RGB images, we calculated MS-SSIM with respect to each RGB channel and reported the average of the values. We evaluated MS-SSIMs at multiple compression rates to draw the rate-distortion trade off curve (RD-curve). For this evaluation, we used Kodak and RAISE-1k (Dang-Nguyen et al., 2015) dataset. The Kodak dataset consists of 24 natural images of size 512×768 , and the RAISE-1k dataset consists of 1K natural images of various image sizes. All of the original RAISE-1k image sizes are exceedingly large, which prevents the evaluation of the MS-SSIM scores in a reasonable computation time. Thus, we resized

and center-cropped each original image as pre-processing. Subsequently, we evaluated the 512×768 and 768×512 pre-processed images.

We calculated bits-per-pixel (bpp) for each method via observing the actual file size of the binary variables. Although the compressed file may possess included meta-information, we did not remove it, assuming the size of the meta-information was negligible, compared to the size of the main body of the binary file.

B.2. Architecture

The proposed lossy autoencoder was composed of 6 convolutional layers and we extracted the quantized variables at four deepest layers as shown in Fig. 13. The number of feature maps (i.e., the number of channels $C^{(i)}$) of each $z^{(i)}$ varied at each compression rate. The number is optimized as follows. First, we set the number of channels at the deepest layer as 32. Subsequently, the number of channels at the shallower layer is set so that it gradually decreases as the layer becomes shallow. Because the number of pixels (i.e., $H^{(i)} \times W^{(i)}$) is four times larger than that of the adjacent higher layer, we search around $C^{(i)} \approx C^{(i+1)}/4$ to maintain similar amount of information (i.e., $C^{(i)} \times H^{(i)} \times W^{(i)} \approx C^{(i+1)} \times H^{(i+1)} \times W^{(i+1)}$) at each layer. For accuracy, $C^{(i)}$ were optimized from $C^{(i)} \in [0, C^{(i+1)}]$. We also optimized the quantization level. The quantization level was selected either 7 or 13 irrelevant to the layer. We select 7 at low-bit-rate coding while we select 13 at high-bit-rate coding. The quantization level and the number of channels used to reproduce the RD curve of the proposed method in Figs. 1 and 8 are summarized in Table 1.

As for the parallel multi-scale lossless coder, we used a CNN with 4 convolution layers, which we call a block, to approximate each $p(v_i^{(k)} | v^{(1)}, \dots, v^{(k-1)})$ ($k = 2, \dots, K$) in Eq. (11). We select the number of blocks K from $\{8, 10, 12\}$ depending on the bitrate. Note that a pair of blocks corresponds to the conditional lossless coder whose coding process is depicted in Fig. 7(d).

At the test phase, we tested two architectures; the one consists of an identical architecture with that used in the training, and the other consists of a smaller architecture where the last two blocks of the architecture used in the training are not used, i.e., the number of blocks are $K - 2$ where K is the number of blocks used during the training. Hence $z^{(1)}$ at the test phase is denser than that of $z^{(1)}$ at the training phase, and the denser $z^{(1)}$ at the test phase is encoded as s using the independent lossless coder. The latter architecture could deteriorate the compression rate because it does not consider the correlation among the denser pixels and the testing condition is different from the training condition. However, we observed that the latter model does not decrease

the compression rate considerably while it exhibits faster encoding/decoding. Therefore, we present the experimental results of the latter model.

B.3. Training

We trained each model with 100,000 updates using mini-batch stochastic gradient descent. The batchsize was 24 for the lossy autoencoder and 6 for the lossless coder. We used Adam optimizer (Kingma & Ba, 2015) with the hyperparameters, $\alpha = 0.001$, $\beta_1 = 0.9$, and $\beta_2 = 0.999$. We also applied linear decay for the learning rate, α , after 75,000 iterations so that the rate would be 0 at the end.

C. Examples of reconstruction images

Figs. 14 and 15 show the reconstructed images obtained with different compression methods. From left to right, we demonstrate the reconstructed images with JPEG, WebP, BPG, and our proposed method. Owing to the size limitation of the supplemental file, we compress each reconstructed images via JPEG with the highest quality.

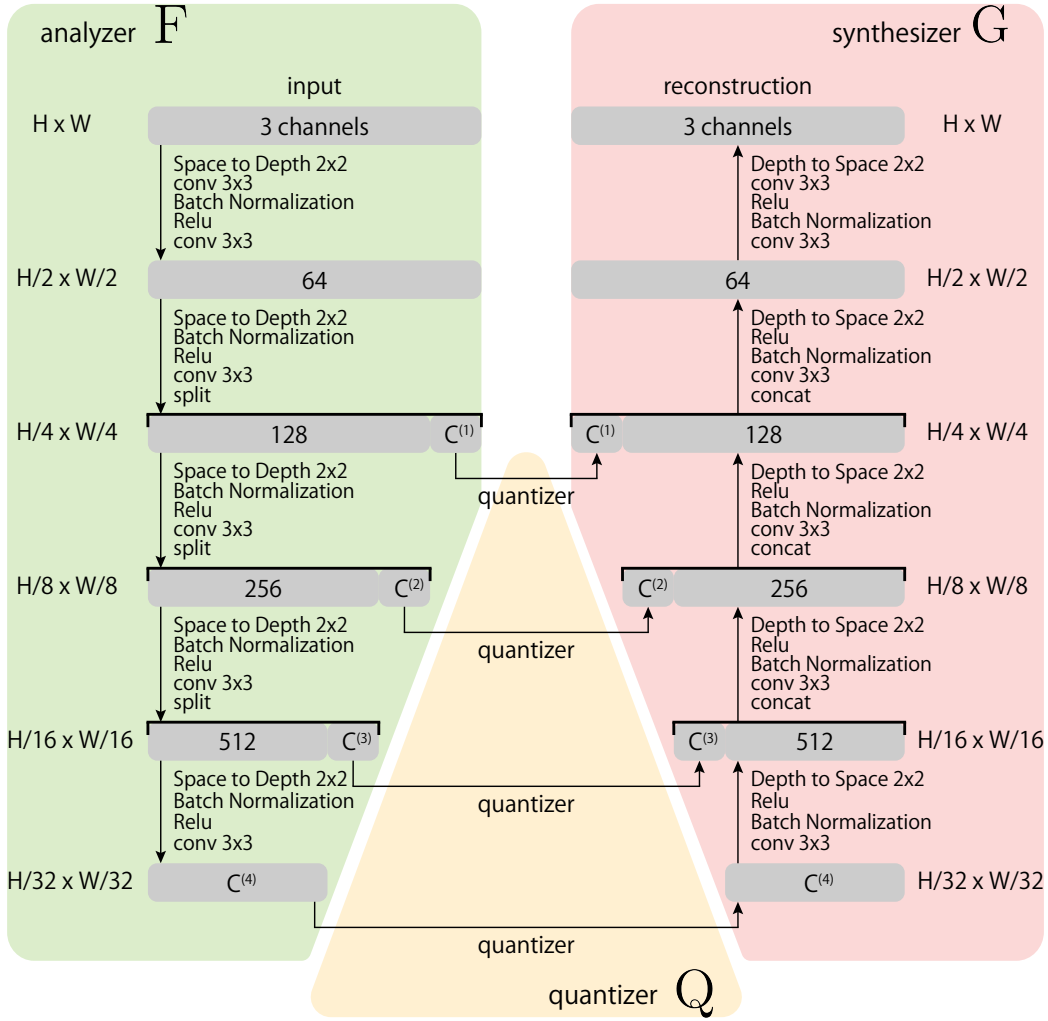


Figure 13. Architecture of lossy autoencoder

Kodak		RAISE-1K		quantization level	$C^{(1)}$	$C^{(2)}$	$C^{(3)}$	$C^{(4)}$
bpp	MS-SSIM	bpp	MS-SSIM					
0.0582	0.8994	0.0576	0.9032	7	0	0	4	32
0.0775	0.9157	0.0766	0.9195	7	0	1	4	32
0.1146	0.9372	0.1123	0.9396	7	0	2	8	32
0.1517	0.9479	0.1468	0.9494	7	0	3	12	32
0.2292	0.9627	0.2186	0.9636	7	0	5	20	32
0.2942	0.9707	0.2786	0.9711	7	1	4	24	32
0.4256	0.9795	0.3987	0.9793	7	2	8	24	32
0.5939	0.9864	0.5567	0.9858	13	2	8	24	32
0.7680	0.9894	0.7166	0.9890	13	3	12	24	32
1.0925	0.9924	1.0289	0.9917	13	5	20	24	32

Table 1. Bits-per-pixel (bpp) and MS-SSIM on RD curve of the proposed method in Figs. 1 and 8. The corresponding hyperparameters (quantization level and number of channels) of the architecture used for the compression are also shown in the right column.

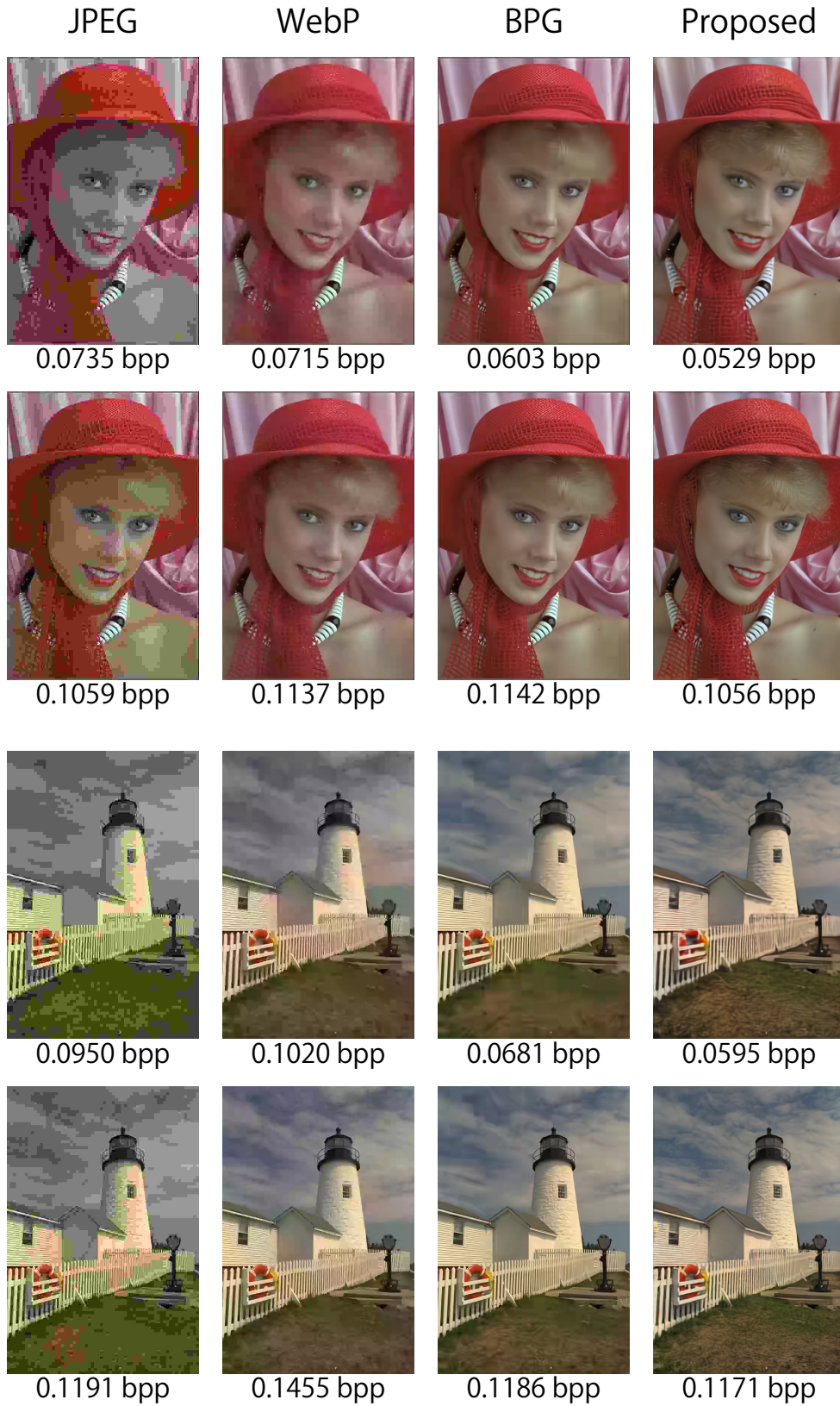


Figure 14. Comparison of reconstruction images of size 768×512 . The number at the bottom of each panel indicates bit-per-pixel (bpp) of each reconstructed image.

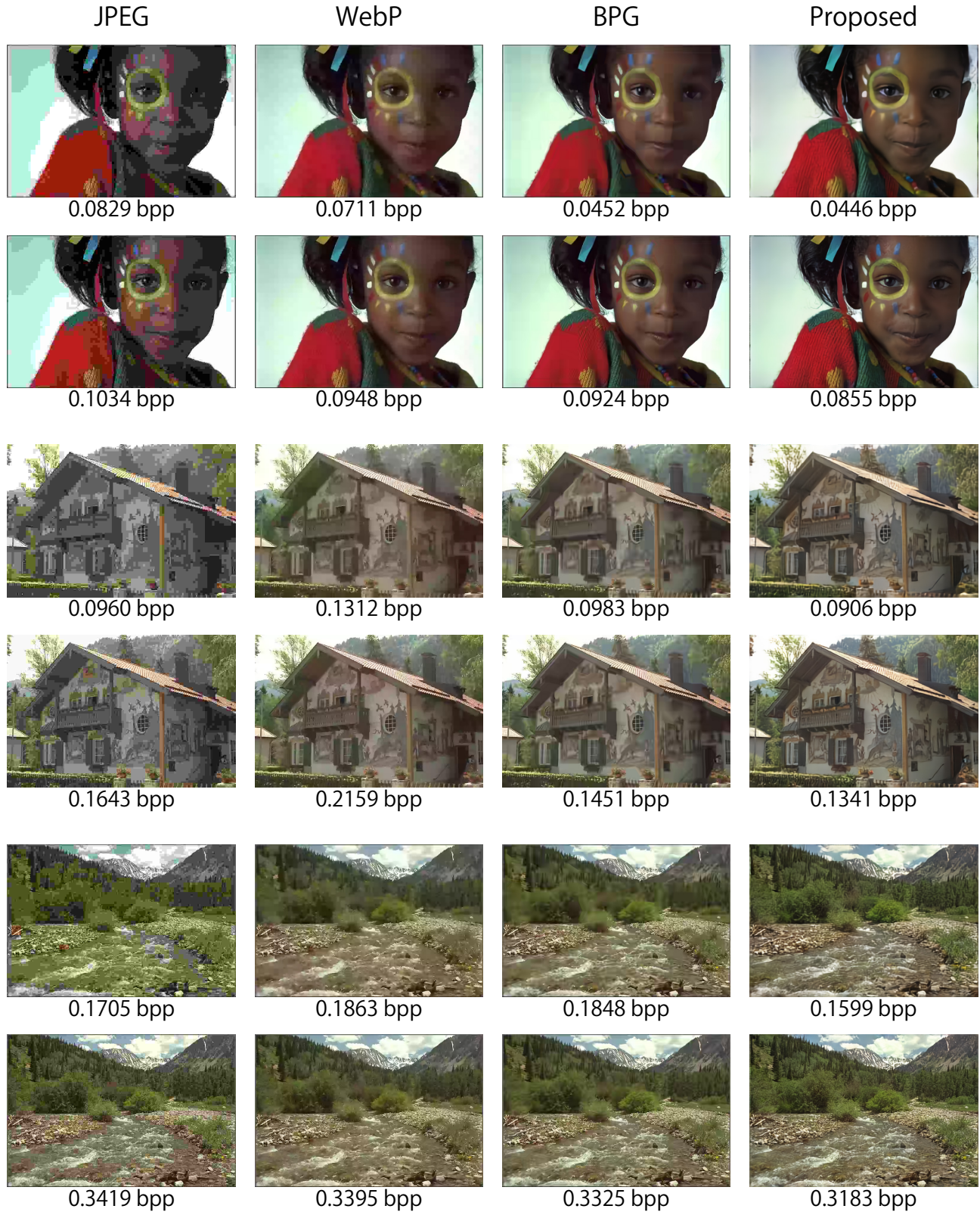


Figure 15. Comparison of reconstruction images of size 512×768 . The number at the bottom of each panel indicates bit-per-pixel (bpp) of each reconstruction